

Pulsed Accretion in a Variable Protostar

James Muzerolle¹, Elise Furlan², Kevin Flaherty³, Zoltan Balog⁴, Robert Gutermuth⁵

¹ *Space Telescope Science Institute, 3700 San Martin Dr., Baltimore, MD 21218, USA*

² *National Optical Astronomy Observatory, Tucson, AZ, 85719, USA*

³ *Steward Observatory, 933 N. Cherry Ave., The University of Arizona, Tucson, AZ 85721, USA*

⁴ *Max-Planck-Institut für Astronomie, Königstuhl 17, 69117, Heidelberg, Germany*

⁵ *Department of Astronomy, University of Massachusetts, Amherst, MA 01003, USA*

Periodic increases in luminosity arising from variable accretion rates have been predicted for some close pre-main sequence binary stars as they grow from circumbinary disks¹⁻³. The phenomenon is known as "pulsed accretion" and can affect the orbital evolution and mass distribution of young binaries^{2,4}, as well as the potential for planet formation in the circumbinary environment^{5,6}. Accretion variability is a common feature of young stars, with a large range of amplitudes and timescales as measured from multi-epoch observations at optical^{7,8} and infrared⁹⁻¹³ wavelengths. Periodic variations consistent with pulsed accretion have been seen in only a few young binaries via optical accretion tracers¹⁴⁻¹⁶, albeit intermittently with accretion luminosity variations ranging from 0-50 percent from orbit to orbit. Here we report on a young protostar (age $\sim 10^5$ yr) that exhibits periodic variability in which the infrared luminosity increases by a factor of 10 in roughly one week every 25.34 days. We attribute this to pulsed accretion associated with an unseen binary companion. The strength and regularity of this accretion signal is surprising; it may be related to the very young age of the system, which is a factor of ten younger than the other pulsed accretors previously studied.

We obtained multi-epoch mid-infrared (MIR) observations of the star forming region IC 348 using the Spitzer Space Telescope. Among the roughly 300 pre-main sequence objects in the cluster, the protostar LRL 54361 (hereafter, L54361) exhibits by far the largest MIR flux variability. We have a total of 81 separate observations of L54361 taken with all three instruments on board Spitzer. The multi-epoch spectral energy distribution (SED) is shown in Figure 1. The measured bolometric luminosity of the system ranges from about 0.2 to 2.7 L_{\odot} . The spectral shape remains relatively constant over this range, aside from slightly bluer mid-infrared colors at higher luminosities.

The photometric light curve indicates that the flux variations occur repeatedly throughout the 7-year span of our observations. The two longest contiguous sets of photometry (Figure 2) reveal a strong pulse signature in which the flux increases by about 2 magnitudes in as little as a few days, followed by a longer exponential decay over the following few weeks. The combined photometric dataset suggests that the variability of L54361 is periodic in nature; the pulse shape revealed by the contiguous warm Spitzer photometry appears in the older data and at other wavelengths, albeit with variations in the pulse width and peak flux. Using several statistical tests, we find that the flux peaks repeat with a robust period of 25.34 ± 0.01 days.

Follow-up multi-epoch imaging taken with the Hubble Space Telescope at near infrared wavelengths reveals spatially-resolved scattered light structures associated with L54361 (Figure 3). The central source varies with almost the same amplitude and light curve shape at 1.6 microns as seen in the Spitzer data, and the peak occurs exactly as expected given the previously determined period. The geometry of the scattered light is similar to that of other protostars¹⁷, and is likely produced by cavities carved out of an infalling envelope by one or more outflows. The apparent motion of the scattered light indicates a light echo produced as the pulse peak light travels through the outflow cavities, and suggests that the source of the illumination is relatively isotropic.

There are three primary sources of periodicity in YSOs: stellar rotation, Keplerian rotation of an inner disk, and the orbital motion of a close binary companion. Stellar rotation can manifest itself via localized hot or cool spots, or via interactions between the stellar magnetic field and the inner disk. In the case of L54361, we reject stellar rotation effects on several grounds: 1) rotation periods for pre-main sequence stars range from a few days to two weeks¹⁸ (and protostars are typically faster still¹⁹), all lower than the measured period; 2) dark spots produce sinusoidal light curves, with amplitudes of a few tenths of a magnitude in the optical and declining to longer wavelengths; 3) hot spots tend to produce less obvious periodicity owing to the more stochastic nature of accretion, and can exhibit phase-dependent asymmetric illumination of the circumstellar material as they rotate with the star²⁰, which we do not see.

Regarding phenomena related to Keplerian rotation of an inner disk, persistent asymmetric structures such as warps in the inner disk can produce periodic obscuration of both single stars⁷ and binary systems^{21,22}. We argue that the data are not consistent with this scenario in several respects: 1) obscuration localized to the disk plane would not affect light propagating in the perpendicular direction through the outflow cavity; 2) obscuration events produce characteristic light curve “dips”, while we see a positive pulse-like shape; 3) as we show below, the MIR and far-infrared flux of L54361 originates mostly in the infalling envelope, whose total flux would not be significantly affected by localized stellar obscuration.

The third possibility, a connection to binary motion, is plausible in terms of the length of the period of L54361, although we do not yet have direct evidence of a companion. The pulsed accretion scenario could explain both the light curve shape and amplitude. Circumbinary disk simulations consistently show gap-clearing by gravitational torques, followed by accretion streams that feed material onto the central stars¹⁻³. For certain binary architectures, particularly in the case of a highly eccentric orbit, the stellar accretion depends on orbital phase, with the highest accretion rates typically associated with periastron passages. A qualitatively similar process has also been suggested for some X-ray binaries, at least one of which has exhibited optical light curves similar to the MIR behavior of L54361^{23,24}.

An increase in the accretion luminosity as a result of the binary interaction increases the irradiation heating of circumstellar dust, which then reradiates the energy in the MIR where we observe it. To help test this hypothesis against our observations, we calculated radiative transfer models of protostellar dust emission and scattering²⁵. The models include three components that are typical of protostellar systems: infalling envelope, accretion disk, and central star. Holding all parameters fixed except for the accretion luminosity, we are able to match the change

between SEDs corresponding to two different pulse phases (Figure 4). The models show a relatively weak wavelength dependence as a function of luminosity, with a slightly flatter spectral slope at about 15 to 70 microns at higher luminosity as a result of optical depth effects in the envelope, in relatively good agreement with the observations.

We do not yet have any direct measure of the central object or its multiplicity status. As our models show, however, the bolometric luminosity provides an estimate of the stellar plus accretion luminosity. Assuming that the low end of the measured range is representative of the stellar luminosity, the combined stellar mass can be roughly estimated by comparing to a theoretical protostellar birthline²⁶ on an Hertzsprung-Russell diagram. We derive a value of $\sim 0.2 M_{\odot}$ (probably an upper limit because some contribution from accretion is likely, although the luminosity may also be somewhat underestimated because of scattering). Conversely, assuming that the upper end of the range of measured luminosity is due entirely to accretion luminosity and adopting the above stellar mass, we derive a maximum mass accretion rate of $10^{-6} M_{\odot} \text{ yr}^{-1}$. This is at the upper end of the range of values measured from standard accretion diagnostics²⁷. Spectroscopic observations are needed to verify an accretion signature, as well as characterize the binary orbit.

Why L54361 exhibits such a strong and regular signature, unlike the T Tauri-type pulsed accretors observed previously, remains unknown. There may be a connection to its earlier evolutionary stage, in which the infalling envelope provides a steady supply of material to the circumbinary disk. By contrast, T Tauri binaries are older by about a factor of ten, have long since dissipated their natal envelopes, and accrete at lower mean rates. Perhaps stochastic variability from other sources such as stellar magnetic interactions or disk turbulence can overwhelm the periodic signature in older stars. It is also possible that the particular orbital parameters of L54361 are rare but more favorable for modulating the accretion flow, such as a very large eccentricity.

References

1. Artymowicz, P. & Lubow, S. H. Dynamics of binary-disk interaction. 1: Resonances and disk gap sizes. *Astrophys. J.* 421, 651-667 (1994)
2. Artymowicz, P. & Lubow, S. H. Mass Flow through Gaps in Circumbinary Disks. *Astrophys. J.* 467, L77-L80 (1996)
3. Gunther, R. & Kley, W. Circumbinary disk evolution. *Astron. Astrophys.* 387, 550-559 (2002)
4. Shi, J., Krolik, J. H., Lubow, S. H., & Hawley, J. F. Three Dimensional MHD Simulation of Circumbinary Accretion Disks: Disk Structures and Angular Momentum Transport. *Astrophys. J.*, 749, 118-144 (2012)
5. Quintana, E. V. & Lissauer, J. J. Terrestrial planet formation surrounding close binary stars. *Icarus* 185, 1-20 (2006)
6. Paardekooper, S.-J., Thebault, P., & Mellema, G. Planetesimal and gas dynamics in binaries. *Mon. Not. R. Astron. Soc.* 386, 973-988 (2008)
7. Bouvier, J. et al. Magnetospheric accretion-ejection processes in the classical T Tauri star AA Tauri. *Astron. Astrophys.* 463, 1017-1028 (2007)
8. Nguyen, D. C., Scholz, A. van Kerkwijk, M. H., Jayawardhana, R., & Brandeker, A. How Variable is Accretion in Young Stars? *Astrophys. J.* 694, L153-L157 (2009)
9. Flaherty, K., Muzerolle, J., Rieke, G., Gutermuth, R., Balog, Z., Herbst, W., Megeath, S. T., & Kun, M. Infrared Variability of Evolved Protoplanetary Disks: Evidence for Scale Height Variations in the Inner Disk. *Astrophys. J.* 748, 71-100 (2012)
10. Morales-Calderón, M. et al. Ysovar: The First Sensitive, Wide-area, Mid-infrared Photometric Monitoring of the Orion Nebula Cluster. *Astrophys. J.* 733, 50-59 (2011)
11. Liu, M. C. et al. Mid-Infrared Imaging of Young Stellar Objects. *Astrophys. J.* 461, 334-344 (1996)
12. Barsony, M., Ressler, M. E., & Marsh, K. A. A Mid-Infrared Imaging Survey of Embedded Young Stellar Objects in the ρ Ophiuchi Cloud Core. *Astrophys. J.* 630, 381-399 (2005)
13. Kóspál, A. et al. The outburst and nature of two young eruptive stars in the North America/Pelican Nebula Complex. *Astron. Astrophys.* 527, A133 (2011)
14. Basri, G., Johns-Krull, C. M., & Mathieu, R. D. The Classical T Tauri Spectroscopic Binary DQ Tau. II. Emission Line Variations with Orbital Phase. *Astron. J.* 114, 781-792 (1997)
15. Mathieu, R. D., Stassun, K., Basri, G., Jensen, E. L. N., Johns-Krull, C. M., Valenti, J. A., & Hartmann, L. W. The Classical T Tauri Spectroscopic Binary DQ Tau. I. Orbital Elements and Light Curves. *Astron. J.* 113, 1841-1854 (1997)
16. Jensen, E. L. N., Dhital, S., Stassun, K. G., Patience, J., Herbst, W., Walter, F. M., Simon, M., & Basri, G. Periodic Accretion from a Circumbinary Disk in the Young Binary UZ Tau E. *Astron. J.* 134, 241-251 (2007)
17. Stark, D. P., Whitney, B. A., Stassun, K., & Wood, K. Near-Infrared Synthetic Images of Protostellar Disks and Envelopes. *Astrophys. J.* 649, 900-913 (2006)
18. Nordhagen, S., Herbst, W., Rhode, K. L., & Williams, E. C. The Variability and Rotation of Pre-Main-Sequence Stars in IC 348: Does Intracluster Environment Influence Stellar Rotation? *Astron. J.* 132, 1555-1570 (2006)
19. Covey, K. R., Greene, T. P., Doppmann, G. W., & Lada, C. J. The Angular Momentum Content and Evolution of Class I and Flat-Spectrum Protostars. *Astron. J.* 129, 2765-2776 (2005)

20. Wood, K. & Whitney, B. Scattered Light Signatures of Magnetic Accretion in Classical T Tauri Stars. *Astrophys. J.* 506, L43-L45 (1998)
21. Herbst, W., LeDuc, K., Hamilton, C. M., Winn, J. N., Ibrahimov, M., Mundt, R., Johns-Krull, C. M. The Light Curve of the Weakly Accreting T Tauri Binary KH 15D from 2005-2010: Insights into the Nature of its Protoplanetary Disk. *Astron. J.* 140, 2025-2035 (2010)
22. Plavchan, P., Gee, A. H., Stapelfeldt, K., & Becker, A. The Peculiar Periodic YSO WL 4 in ρ Ophiuchus. *Astrophys. J.* 684, L37-L40 (2008)
23. Skinner, G. K. Observations of optical flares in the recurrent X-ray transient A0538-66. *Nature* 288, 141-143 (1980)
24. Densham, R. H., Charles, P. A., Menzies, J. W., van der Klis, M., & van Paradijs, J. Four outburst cycles of A0538-66: evidence for a rapidly evolving envelope around the primary. *Mon. Not. R. astr. Soc.* 205, 1117-1133 (1983)
25. Kenyon, S. J., Calvet, N., & Hartmann, L. The embedded young stars in the Taurus-Auriga molecular cloud. I - Models for spectral energy distributions. *Astrophys. J.* 414, 676-694 (1993)
26. Hartmann, L., Cassen, P., & Kenyon, S. J. Disk Accretion and the Stellar Birthline. *Astrophys. J.* 475, 770-785 (1997)
27. White, R. J. & Hillenbrand, L. A. On the Evolutionary Status of Class I Stars and Herbig-Haro Energy Sources in Taurus-Auriga. *Astrophys. J.* 616, 998-1032 (2004)

Acknowledgements

This work was supported in part by NASA through Spitzer and HST GO contracts. We thank S. Lubow, M. Livio, and N. Calvet for discussions. E. F. was visiting the Infrared Processing and Analysis Center, Caltech, during the course of this work.

Author Contributions

J. M. and K. F. designed the Spitzer observations. Z. B. and R. G. reduced the IRAC images and compiled the photometry, while J. M. reduced and analyzed the MIPS data. J. M. and E. F. extracted and analyzed the IRS spectroscopy. J. M. designed the HST observations and analyzed the images. E. F. calculated the radiative transfer models and fit the observed SEDs. All authors contributed to the writing of the paper.

Author Information

The authors declare no competing financial interests. Correspondence and requests for materials should be addressed to J. M. (muzerol@stsci.edu).

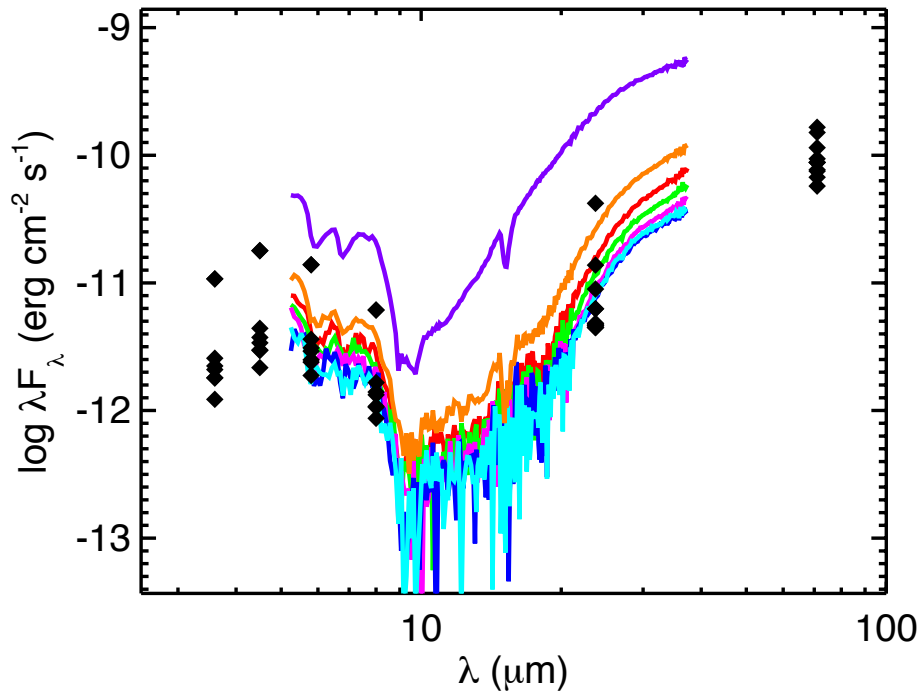


Figure 1. Multi-epoch spectral energy distribution of L54361. Our complete set of observations taken during cryogenic Spitzer operations are shown, including photometry from all four IRAC channels at 3.6 - 8 microns and the MIPS 24 and 70 micron channels (diamonds), as well as 7 epochs of IRS spectroscopy (in chronological order: red, green, magenta, blue, cyan, purple, and orange lines). Each single-epoch SED exhibits a shape characteristic of Class I objects, with the flux rising sharply to longer wavelengths and a strong silicate absorption feature at 8-12 microns. Between epochs, however, the flux varies by as much as an order of magnitude at all wavelengths, with only a slightly shallower spectral slope in the ~ 15 -70 micron continuum as the flux increases.

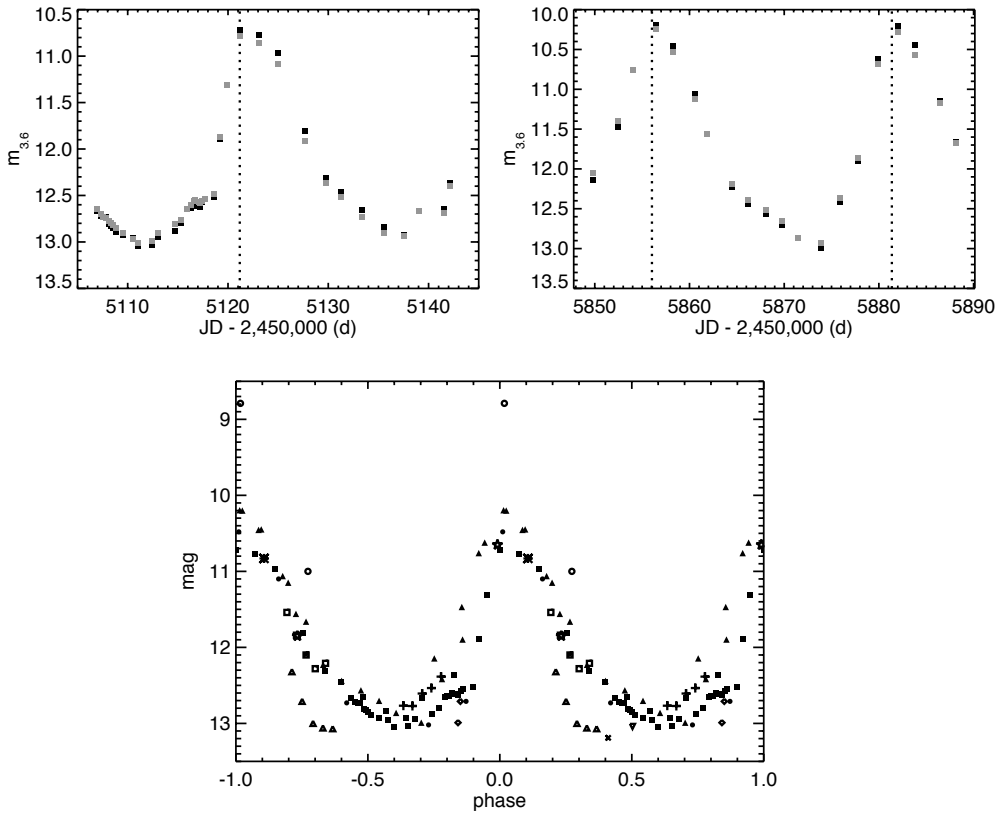


Figure 2. Photometric light curves for L54361. *Upper panels:* IRAC 3.6 (black) and 4.5 (gray, scaled down to match 3.6) micron magnitudes from the fall 2009 (left) and fall 2011 (right) Spitzer observing campaigns. Note that the 3-sigma photometric uncertainties are equal to or smaller than the symbol size. The dashed line in the left panel marks the observed peak time, which we set as the fiducial epoch for phase=0. The dashed lines in the right panel mark the predicted peak times assuming a periodicity of 25.34 days. *Lower panel:* The phased photometric light curve of L54361, assuming a period of 25.34 days and the phase zero epoch JD 2,455,121.203. Included are measurements taken at three separate wavelengths. Each symbol type represents a contiguous set of photometry: cryo-Spitzer IRAC 3.6 microns (plus signs, asterisk, cross), warm Spitzer IRAC 3.6 microns (solid squares, solid triangles), MIPS 24 microns (inverted triangle, open diamonds, open stars, open triangles), IRS 24 microns (open circles, open squares), HST WFC3 1.6 microns (solid circles). The 24 micron photometry are offset by +7.3 magnitudes and WFC3 photometry offset by -5.3 magnitudes in order to place everything on the same scale.

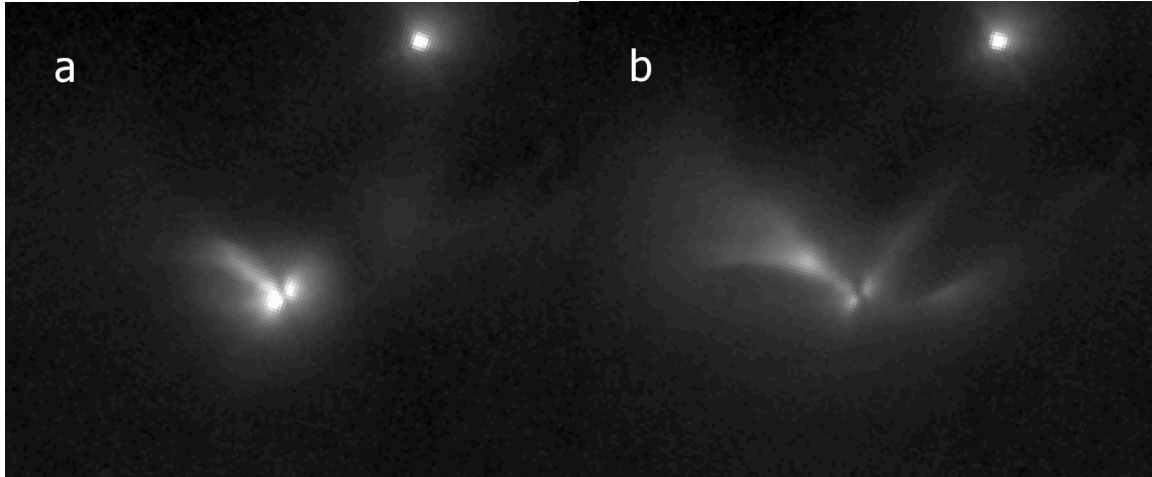


Figure 3. Near-infrared images of L54361. The two panels show portions of images taken with HST/WFC3 at 1.6 microns at two epochs corresponding to pulse phases of 0 (a) and 0.3 (b). North is up and east is to the left. L54361 is the extended source just below the center of the images; the point source at upper right is another YSO, LRL 1843. The light from L54361 subtends roughly $14''$ (~ 4000 AU at the distance of the IC 348 region) in (a), and about $50''$ ($\sim 15,000$ AU) in (b). Most if not all of this light is likely the result of scattering off of circumstellar dust in the protostellar envelope. An apparent edge-on disk is visible at the center of the object, and 3 separate structures indicative of outflow cavities extend to the northwest, southwest, and northeast. The extent and morphology of the scattered light changes substantially between epochs as a result of the propagation of the pulse peak light. (See Supplementary Information for the complete set of HST images.)

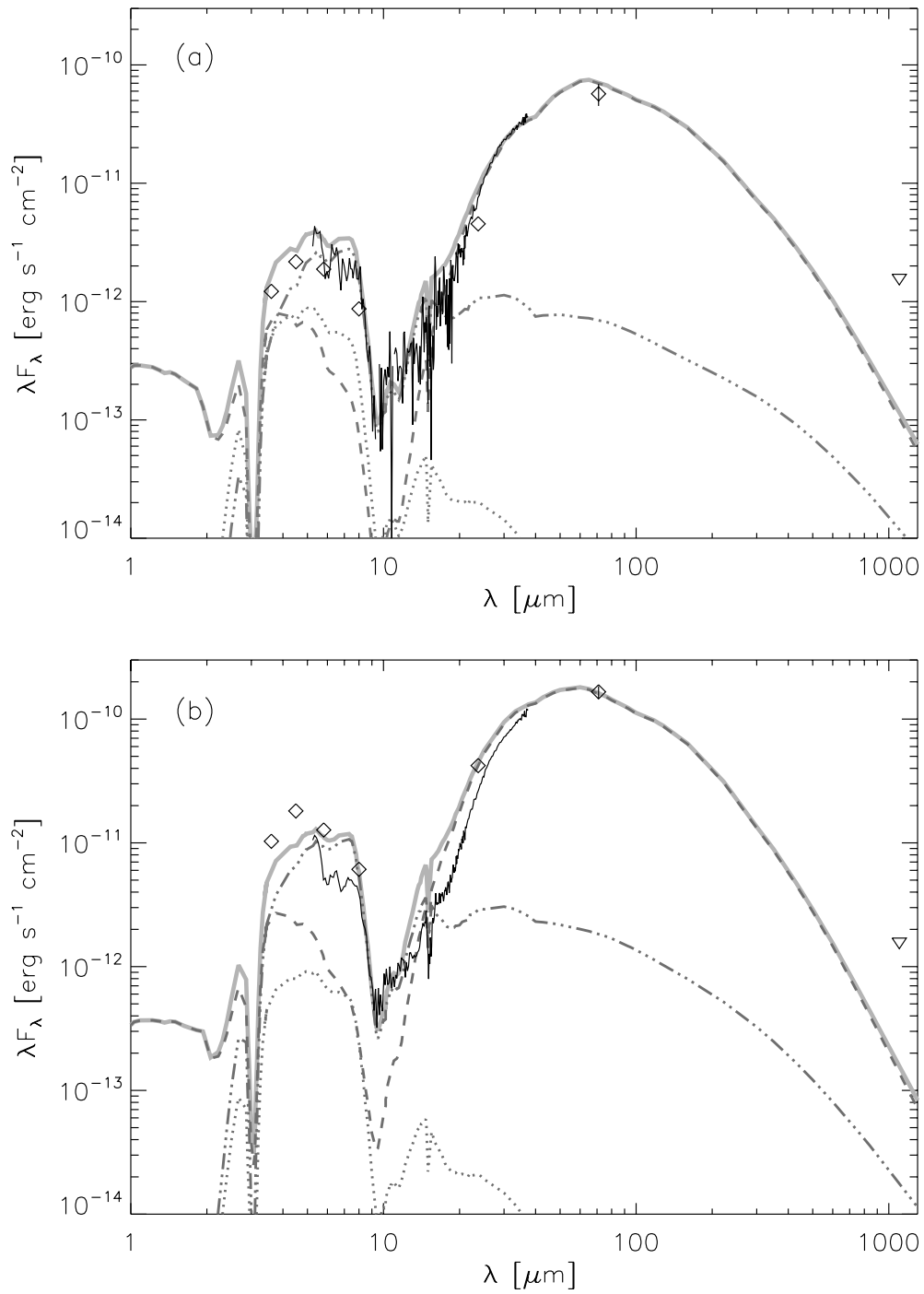


Figure 4. Protostellar spectral energy distribution models for L54361. We compare models to two sets of observations roughly representing pulse phases of 0.4 and 0.15 (top and bottom panel, respectively). The photometry and spectroscopy are not simultaneous but were selected to

correspond roughly to a common flux level. The dashed lines indicate scattering and emission from the infalling envelope; the dash-triple-dotted lines represent scattering and emission from the circumstellar accretion disk; the dotted lines represent reddened flux from the central star; the solid gray line shows the total flux from all these components. The best-fit parameters include an envelope infall rate of $3 \times 10^{-6} M_{\odot} \text{ yr}^{-1}$ (assuming a stellar mass of $0.2 M_{\odot}$), envelope centrifugal radius $R_c = 30 \text{ AU}$, outflow cavity opening angle $\theta = 30^{\circ}$, inclination angle of the outflow/stellar rotation axis to the line of sight $i = 70^{\circ}$, total central luminosity (stellar plus accretion) $L = 0.5 L_{\odot}$ (top panel) and $1.3 L_{\odot}$ (bottom panel), and the fraction of L due to the stellar luminosity $\eta_{star} = 0.5$ (top panel) and 0.19 (bottom panel). The only parameter that was actually changed between the two models was η_{star} , with appropriate values so that the stellar luminosity remained constant while the accretion luminosity changed by a factor of ~ 4 . (See Supplemental Information for details of the model calculations and parameters.)

S1 Supplementary Information

Spitzer Observations & Data Reduction

We observed L54361 with all instruments onboard the Spitzer Space Telescope; Table S1 shows the observation log. IRAC observations obtained during the cryogenic mission comprise all four channels (3.6, 4.5, 5.8, and 8 microns), while the warm operations data comprise only the first two. All frames were processed using the Spitzer Science Center (SSC) IRAC Pipeline v14.0.0, and mosaics were created from the basic calibrated data (BCD) frames using a custom IDL program²⁸. Aperture photometry on these images was carried out using PhotVis version 1.10, which is an IDL GUI-based photometry visualization tool. The relative photometric uncertainties are < 1%. The zero point magnitudes of the calibration were 19.6642, 18.9276, 16.8468, and 17.3909 for channel 1, 2, 3, and 4, respectively. Aperture corrections of 0.21, 0.23, 0.35 and 0.5 mag were applied for channels 1, 2, 3, and 4 to account for the differences between the aperture sizes used for the standard stars and for the IC 348 photometry. We also reprocessed existing archived data, from GTO (PID 6 and 58) and c2d legacy (PID 178) programs, using the same methodology. The photometry is shown in Table S2.

For spectroscopy with the IRS, both Short-Low and Long-Low modules were used in order to cover the full wavelength range, 5 to 40 microns, with spectral resolution $\lambda/\Delta\lambda \sim 60-120$. The observations were performed in staring mode using two cycles of 14 seconds exposure for both modules. The data were reduced using SMART version 8.1.2²⁹, starting with the BCD products from the SSC reduction pipeline version S18.7. The two-dimensional spectra taken at two nod positions were subtracted from each other in order to remove the background. The spectra were then extracted using optimal source extraction³⁰. The residual local sky background (generally very low) was subtracted by fitting a polynomial to the sky pixels on either side of the source at each row in the spatial direction. The final calibrated spectra for each nod and order were then combined using the sigma-clipped averaging function in SMART. Intrinsic measurement uncertainties are about 2% at the highest flux levels, though the S/N is much lower at fainter levels particularly in the region of the 10 micron silicate absorption feature.

The MIPS observations were taken in scan mode using 12 scan legs with 30' length, half-array offsets, and medium scan rate, with coordinates centered on the IC 348 cluster center. Starting with the raw data, individual images were calibrated and mosaicked using the MIPS GTO team Data Analysis Tool version 3.06. Photometry was measured using the daophot PSF fitting routine. We only analyzed the 24 and 70 micron data, as the 160 micron channel was saturated. We also reprocessed existing archived data, from GTO (PID 6 and 58) and c2d legacy (PID 178) programs, using the same methodology. In all images, the relative photometric uncertainties are <1% at 24 microns and ~10% at 70 microns. The photometry is listed in Table S3.

Periodicity Analysis

We considered all Spitzer photometry of L54361 obtained with the IRAC 3.6 micron and MIPS 24 micron channels. In addition, we added 24 micron photometry derived from the IRS data by convolving the spectra with the MIPS filter throughput. A Lomb-Scargle periodogram analysis

of this entire set of photometry shows a significant peak at a period of 25.34 days (Figure S1). This period has a false alarm probability of 2×10^{-8} . As a check, we also ran the same data with the “SigSpec” routine³¹, which is statistically more robust than the Lomb-Scargle periodogram. SigSpec returns a probability of 1.3×10^{-11} that the 25.34-day period is not real. We conservatively estimate an uncertainty on the period determination of 0.01 days, based on the FWHM of the periodogram peak; a formal analysis using traditional periodogram methodology³¹ yields an uncertainty of 0.0007 days.

HST Observations and Analysis

We obtained 7 epochs of imaging with the Hubble Space Telescope WFC3/IR instrument, using the F160W broad band filter. A 4-point dither pattern was used, with exposure times of about 10 minutes per point. The data were processed using the STScI pipeline, including MultiDrizzle combination of individual exposures and subtraction of the mean background level. For comparison with the Spitzer photometry, as shown in Figure 2 of the main text, we measured aperture photometry of the central source using an aperture radius of 1” centered at the position of the MIR source (this includes both scattered light lobes on either side of the apparent edge-on disk) and no background subtraction. Instrumental magnitudes were converted to the Vega system using a zeropoint magnitude of 24.7.

Portions of each image showing the full visible extent of L54361 are shown in Figure S2. The central source is split into two lobes separated by a dark lane indicative of an edge-on disk; it is probably not seen directly but rather via scattered light on both sides of the disk. The extended nebulosity includes three V-shaped structures extending to the northwest, northeast, and southeast (the latter considerably foreshortened), with their vertices meeting approximately at the central position of the MIR source (Figure S3). The morphology of these regions is typical of protostellar sources, and is the likely result of cavities carved out of the protostellar envelope by one or more outflows. Knots of emission likely related to a jet/outflow, most of them seen previously from the ground via molecular hydrogen emission^{33,34}, extend further to the northwest. The different angle of the NE structure suggests either that the outflow opening angle is larger on the east side of the source, or that there is a separate jet/outflow (though one has not been detected directly thus far). There is also a very faint feature in some of the images that appears to connect the NE cavity to the nearby object LRL 1843. This source is a known substellar member of the cluster with a spectral type of M8.75, mass $\sim 0.02 M_{\odot}$, age $< 1 \text{ Myr}$ ³⁵. Whether the two objects are physically related cannot be determined with the current data.

The brightness and physical extent of the scattered light are highly variable, with the nebulosity growing larger in size after the central source reaches its peak flux. These morphological variations strongly suggest the presence of a light echo. Moreover, they also indicate that the illumination resulting from the flux pulses is more or less isotropic, rather than localized as would be expected for a rotating stellar hot spot or an obscuration event associated with the inner disk. We measured photometry at various small apertures spaced with increasing distance from the central source along two different axes roughly corresponding to the NW/SE and NE outflow cavities (Fig. S4). The resultant relative magnitudes are shown for each aperture as a function of observation epoch in Figure S5. The shape and relative amplitude of the pulse are clearly

preserved in all apertures. The timing of the peak flux is shifted to consistently later times as one goes farther from the central source, as expected for a light echo. The lag between the arrival time of light observed from an echo at a projected distance r in arcseconds from the source and light observed directly from the source can be expressed as

$$\Delta t = \frac{rd}{c} \frac{1 - \cos \theta}{\sin \theta}, \quad (1)$$

where θ is the angle of the light echo location relative to the line of sight, and d is the distance to the central source in parsecs³⁶. Using the folded Spitzer IRAC photometry as a proxy for the intrinsic pulse profile from the central source, we can reasonably match most of the HST aperture light curves by applying the appropriate delay times as given by Equation 1, assuming an angle $\theta = 90^\circ$ (i.e., in the plane of the sky) and a distance $d = 250$ pc. The fits to apertures E and F could be improved by adopting $\theta = 70^\circ$; this may indicate that the NE structure is indeed produced by a separate outflow that is tilted more towards the line of sight than the NW/SE outflow (and whose counterflow to the SW is unseen because of obscuration by the disk and envelope). The assumed distance is consistent with the lower end of the range for the IC 348 cluster in the literature (~ 260 to 320 pc)³⁷⁻³⁹. However, we cannot definitively rule out larger values. A more robust distance constraint awaits detailed 3D modeling of the outflow cavity geometry.

Radiative Transfer Models

We calculated models of this protostellar system using a radiative transfer code that treats three separate components: a central protostar, circumstellar disk, and envelope²⁵. The envelope is modeled as a collapsing, slowly rotating, spherically symmetric cloud core (“TSC”)⁴⁰, and the disk as an optically thick, flat disk irradiated by the central star. The disk is a natural outcome of the collapse of a rotating core, with material that is falling in along the equatorial plane landing at the centrifugal radius. In the model calculation, the radiative equilibrium temperature is determined first by using the angle-averaged density distribution in the infall region; at large distances, the envelope is spherically symmetric, but closer to the star the density distribution is flatter since material falls onto the disk. Next, the flux emitted by the system is calculated using the actual flattened, axially symmetric density distribution derived by TSC. Outflow cavities, which follow the streamlines of infalling particles, can also be included in the model. Since there is no material inside the cavity, a large cavity reduces the amount of emitting dust, which for more face-on orientations allows us to see more light from the star and inner disk. In addition, the cavity walls add to scattered light in the near-infrared.

The model parameters that were adjusted to fit observations include the total input luminosity (stellar plus accretion; the latter consists of the accretion luminosity emitted by the disk plus the accretion shock on the stellar surface), the fraction of that luminosity due to the star, the envelope density at a reference radius (which, assuming a mass for the central protostar, can be converted to a mass infall rate²⁵), the centrifugal radius (which is also equal to the outer disk radius), the cavity opening angle and the inclination angle. The stellar radius was assumed to be 2 solar radii, the inner disk radius 3 stellar radii, the outer envelope radius 10000 AU. The dust

was assumed to be composed of small (<0.3 micron) silicate and graphite grains⁴¹, troilite (FeS) and water ice⁴², as well as CO₂ ice⁴³, with abundances similar to the ones adopted in previous models of the well-known protostar L1551 IRS 5⁴⁴. The best-fit parameters were determined by assessing the model fits by eye, after adjusting them based on our extensive previous experience of modeling protostars in the Taurus star-forming region⁴⁵. The near-infrared HST images provided constraints on the inclination and cavity opening angle. The shape of the IRS spectrum in the 15-40 micron region and the 70 micron photometry helped constrain those parameters as well, and more importantly the envelope reference density and centrifugal radius.

Compared to previous model fitting of other protostars, the best-fit models shown in Figure 4 have a relatively small centrifugal radius, typical density, high inclination and large cavity. Lacking direct constraints on the stellar luminosity, we assume it is equal to half the total luminosity in the low flux case; this has at most a small effect on the results since the reddened stellar component is non-negligible only at a narrow range of wavelengths around 3 to 5 microns in the low flux case, and negligible at all wavelengths in the high flux case. Emission from the disk component, attenuated by extinction from envelope dust, dominates the total model flux at 4.5 to 10 microns. The envelope component dominates at wavelengths shorter than 3.6 microns (scattered light) and longer than about 20 microns (dust emission). To match the observed temporal change, we fixed all parameters except for the accretion luminosity, the only parameter for which changes on timescales of weeks are physically plausible.

Table S1 Observation log

instrument	date	reference
Spitzer/IRAC	2004 Feb 11	46
	2004 Sep 8	47
	2009 Mar 18, 19, 20, 21, 22	this work
	2009 Oct 2 - Nov 6	this work
	2011 Oct 15 – Nov 22	this work
Spitzer/MIPS	2004 Feb 21	46
	2004 Sep 19	48
	2007 Sep 23, 24, 25, 26, 27	this work
	2008 Mar 12, 19	this work
Spitzer/IRS	2008 Oct 6, 7, 8, 9, 10	this work
	2009 Mar 3, 10	this work
HST/WFC3	2010 Dec 3, 7, 11, 15, 18, 22, 26	this work

All Spitzer observations obtained prior to May 2009 were taken during cryogenic operations; each date corresponds to a separate observation. The IRAC observations obtained in fall 2009 and fall 2011 were taken during warm operations and only included the first two channels at 3.6 and 4.5 microns; only the range of dates is given, as these consisted of a total of 38 and 20 separate observations, respectively.

Table S2 Spitzer IRAC photometry

MJD (days)	[3.6]	err	[4.5]	err	[5.8]	err	[8]	err
53046.020	10.830	0.005	9.563	0.004	9.070	0.005	8.967	0.006
53256.453	13.190	0.025	11.854	0.028	11.239	0.034	11.088	0.049
54909.242	12.767	0.044	11.509	0.038	10.977	0.045	10.871	0.055
54910.121	12.771	0.041	11.517	0.035	10.932	0.047	10.855	0.053
54911.043	12.607	0.034	11.368	0.027	10.762	0.034	10.628	0.045
54911.938	12.535	0.024	11.262	0.024	10.698	0.035	10.572	0.044
54912.863	12.385	0.023	11.084	0.020	10.530	0.027	10.388	0.028
55106.898	12.682	0.015	11.379	0.035				
55108.129	12.798	0.041	11.467	0.052				
55109.574	12.911	0.064	11.607	0.045				
55110.496	12.993	0.063	11.685	0.044				
55111.062	13.056	0.066	11.720	0.046				
55112.430	13.054	0.029	11.722	0.043				
55113.066	12.967	0.045	11.614	0.038				
55114.727	12.893	0.032	11.545	0.031				
55115.363	12.840	0.038	11.461	0.028				
55115.961	12.685	0.029	11.349	0.025				
55117.125	12.607	0.022	11.292	0.022				
55118.598	12.521	0.020	11.193	0.019				
55119.246	11.943	0.014	10.605	0.012				
55119.926	11.333	0.010	10.036	0.008				
55107.293	12.728	0.039	11.419	0.044				
55107.570	12.756	0.037	11.406	0.052				
55107.805	12.776	0.046	11.451	0.041				
55108.379	12.804	0.045	11.493	0.052				
55108.574	12.820	0.044	11.526	0.049				
55108.809	12.876	0.051	11.559	0.052				
55116.312	12.650	0.024	11.305	0.022				
55116.613	12.654	0.021	11.261	0.023				
55116.715	12.627	0.030	11.289	0.021				
55117.207	12.623	0.031	11.292	0.021				
55117.457	12.581	0.027	11.277	0.017				
55117.688	12.590	0.024	11.246	0.022				
55123.066	10.800	0.008	9.550	0.007				
55124.953	11.023	0.011	9.804	0.009				
55127.672	11.871	0.022	10.623	0.024				
55129.805	12.329	0.030	11.083	0.029				
55131.270	12.482	0.036	11.224	0.036				
55133.375	12.681	0.035	11.432	0.043				
55135.605	12.861	0.049	11.619	0.041				

Table S2 Spitzer IRAC photometry

55137.516	12.934	0.050	11.663	0.037
55139.059	12.675	0.025	11.382	0.027
55141.508	12.708	0.033	11.415	0.028
55142.109	12.407	0.020	11.127	0.022
55121.203	10.732	0.006	9.493	0.005
55849.770	12.134	0.018	10.856	0.020
55852.410	11.452	0.014	10.194	0.010
55854.035	10.782	0.008	9.544	0.007
55856.422	10.212	0.006	9.022	0.005
55858.234	10.515	0.009	9.343	0.007
55860.555	11.113	0.017	9.909	0.016
55861.828	11.578	0.025	10.374	0.020
55864.434	12.251	0.042	10.991	0.040
55866.211	12.459	0.041	11.173	0.038
55868.066	12.582	0.040	11.297	0.043
55869.809	12.717	0.048	11.461	0.040
55871.445	12.928	0.055	11.633	0.042
55873.859	13.020	0.039	11.728	0.033
55875.852	12.461	0.020	11.149	0.018
55877.824	11.903	0.011	10.665	0.010
55879.949	10.623	0.006	9.451	0.006
55882.020	10.210	0.005	9.094	0.005
55883.836	10.505	0.007	9.369	0.007
55886.422	11.132	0.017	9.971	0.016
55888.137	11.692	0.025	10.488	0.028

All entries with missing 5.8 and 8 micron photometry correspond to data taken during warm operations.

Table S3 Spitzer MIPS photometry

MJD (days)	[24]	err	[70]	err
53056.062	5.79	0.05	-1.07	0.18
53267.371	5.70	0.05	-0.92	0.21
53267.594	5.42	0.06		
54366.379	5.03	0.05	-1.36	0.13
54367.355	5.42	0.05	-1.14	0.17
54368.406	5.72	0.05	-0.90	0.24
54369.355	5.78	0.05	-0.60	0.22
54370.301	5.79	0.04	-0.78	0.21
54538.156	3.36	0.04	-1.65	0.10
54544.285	4.57	0.04	-1.76	0.12

The third entry contains no 70 micron data because the scan pattern has a gap at the position of the source.

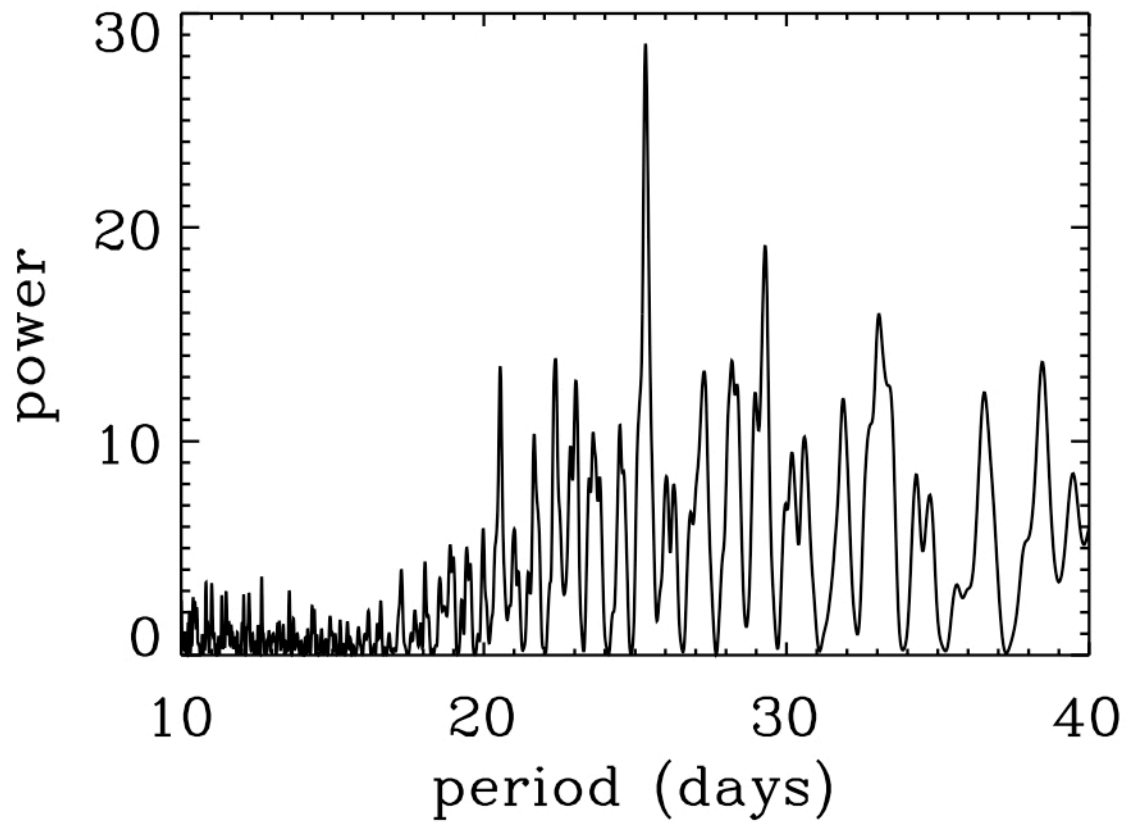


Figure S1. The Lomb-Scargle periodogram corresponding to the Spitzer photometry of LRL 54361. The peak power corresponds to a period of 25.34 days.

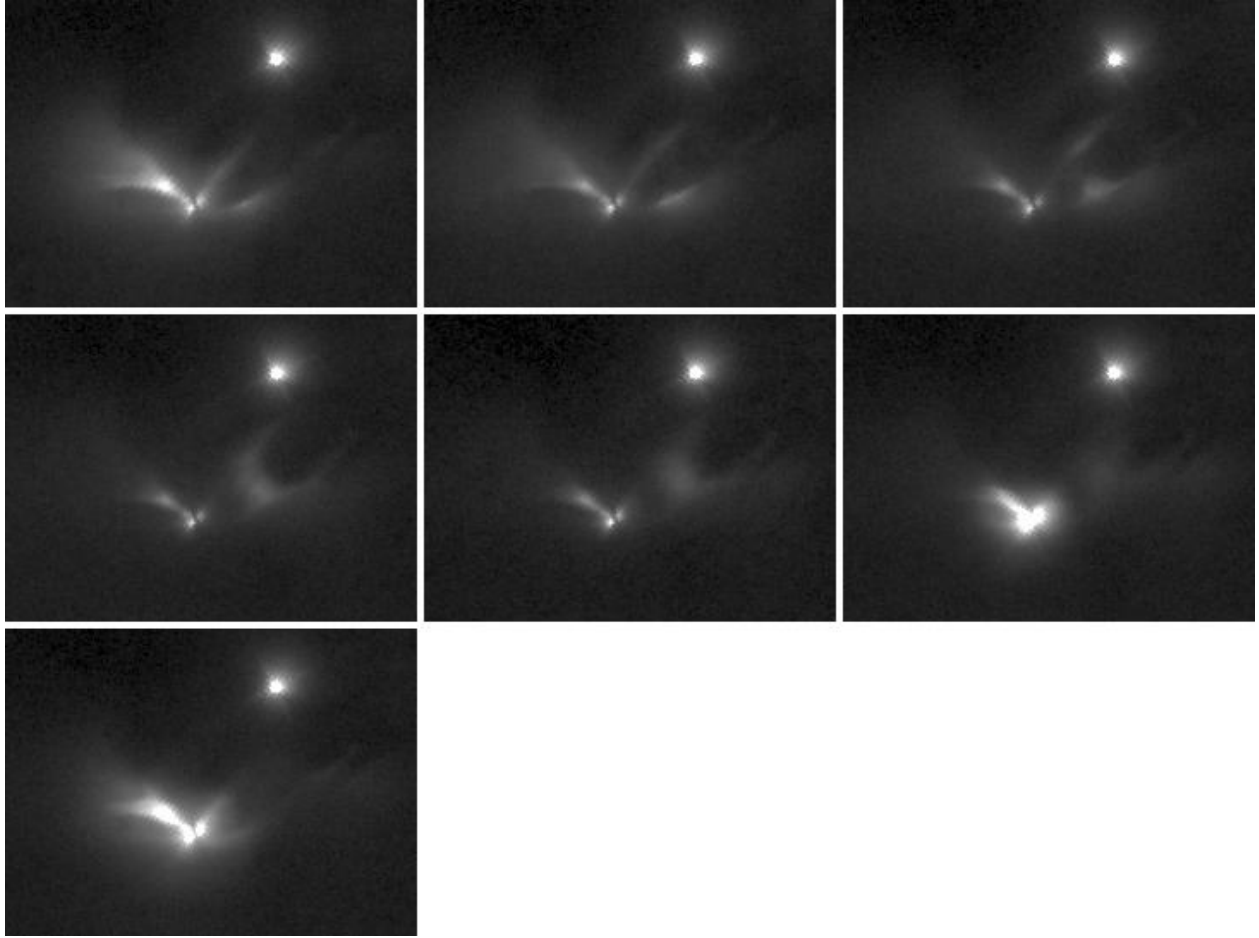


Figure S2. A montage of the HST/WFC3 F160W images, centered roughly on L54361 (only a portion of the full images are shown). North is up, east is to the left. Each panel spans about $25'' \times 20''$. The observations are separated by about 3 - 4 days (see Table 1); time proceeds from left to right, top to bottom. Another cluster member, LRL 1843, is seen at upper right.

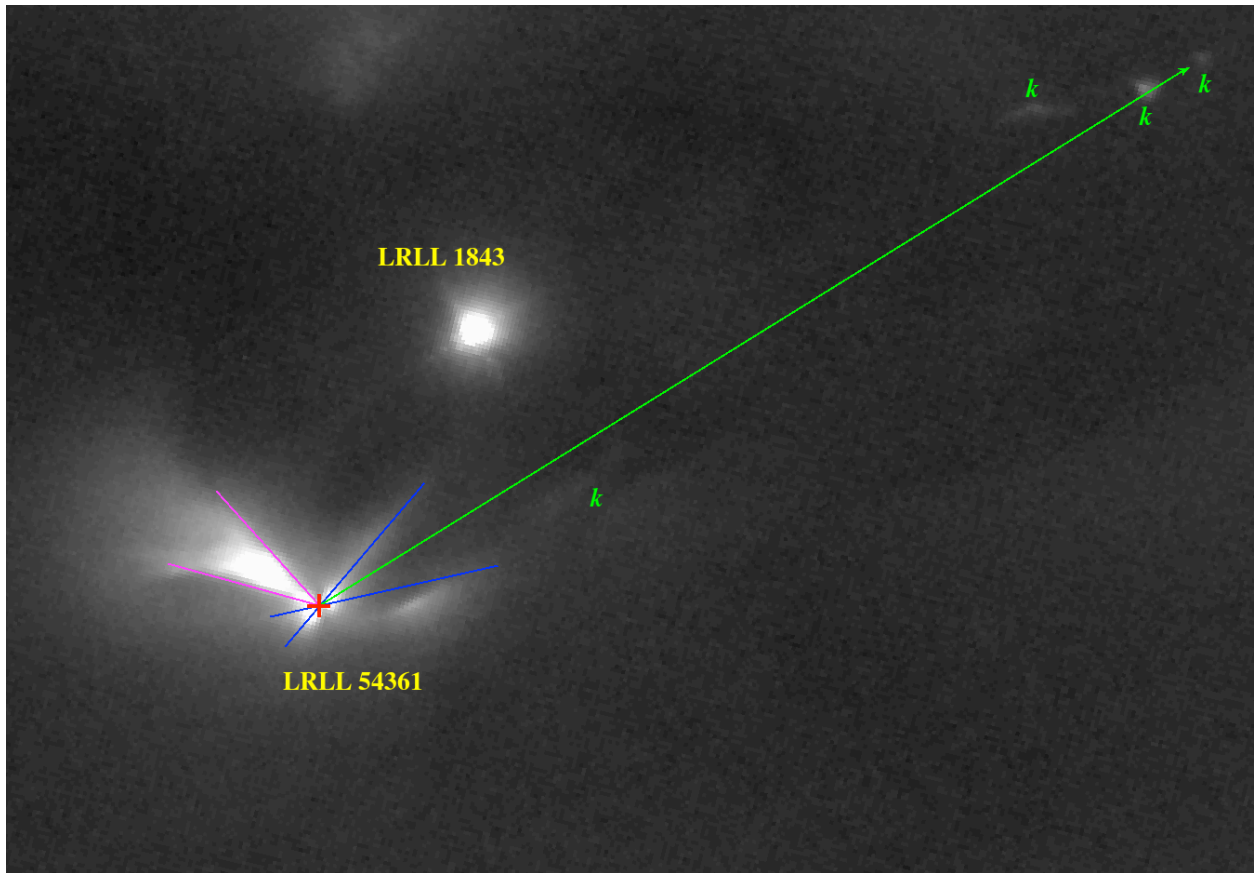


Figure S3. Geometry of the L54361 system. The grayscale image is from the HST/WFC3 epoch 1 image. The red cross marks the centroid position of the Spitzer/IRAC source. The blue lines mark the approximate boundaries of the NW/SE outflow cavities. The magenta lines mark the rough boundaries of a separate scattered light region that may be a cavity produced by a second misaligned outflow, or possibly an asymmetric extension of the SE outflow cavity. The green arrow indicates the general direction of the NW jet, with individual knots marked with a “k” (note that the positions and morphologies of these do not change with time). The brown dwarf cluster member LRL 1843 is also labeled.

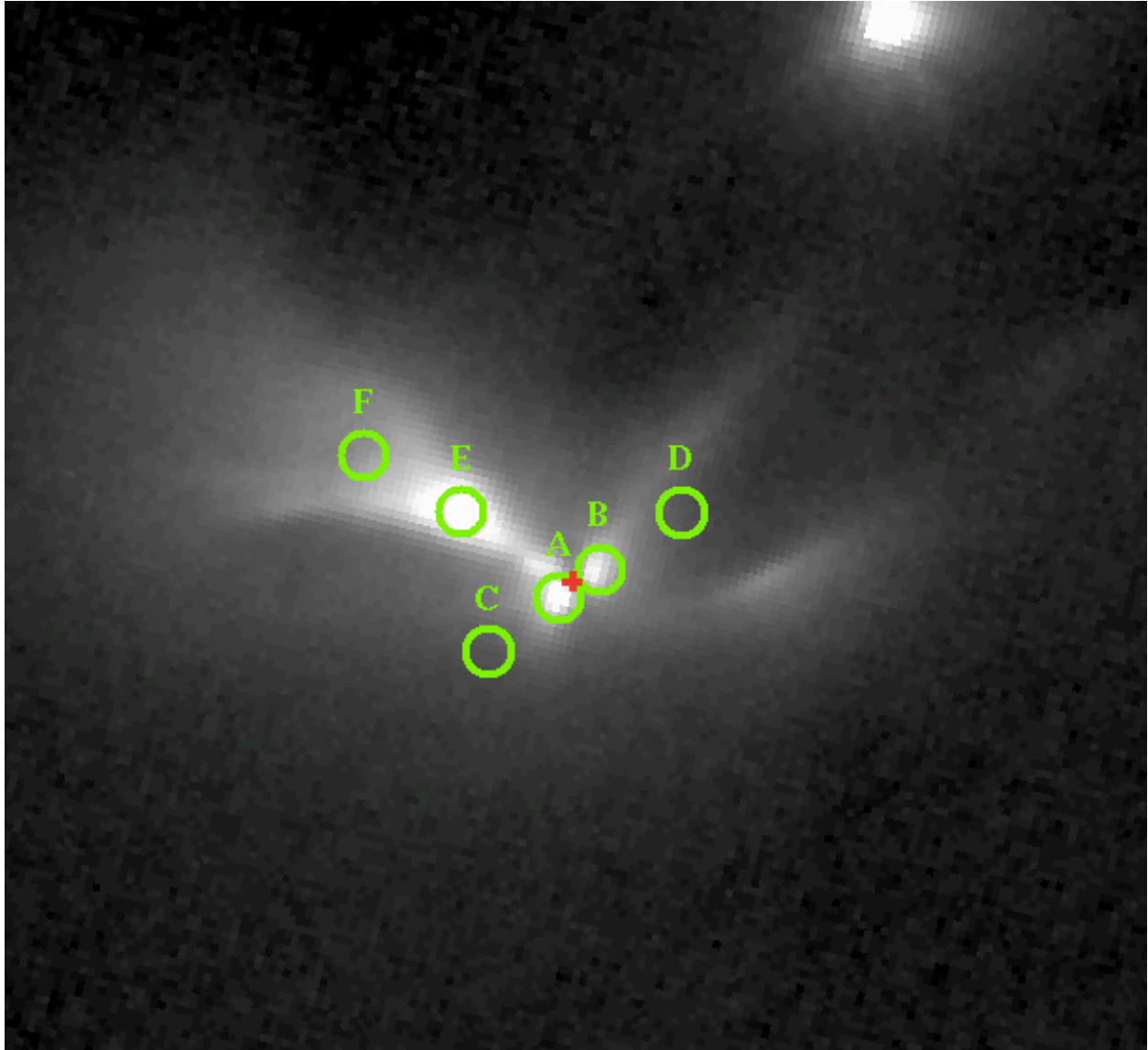


Figure S4. Close-up of the epoch 1 HST/WFC3 image. The red cross marks the centroid position of the Spitzer source. The green circles mark the six regions of aperture photometry shown in Figure S5.

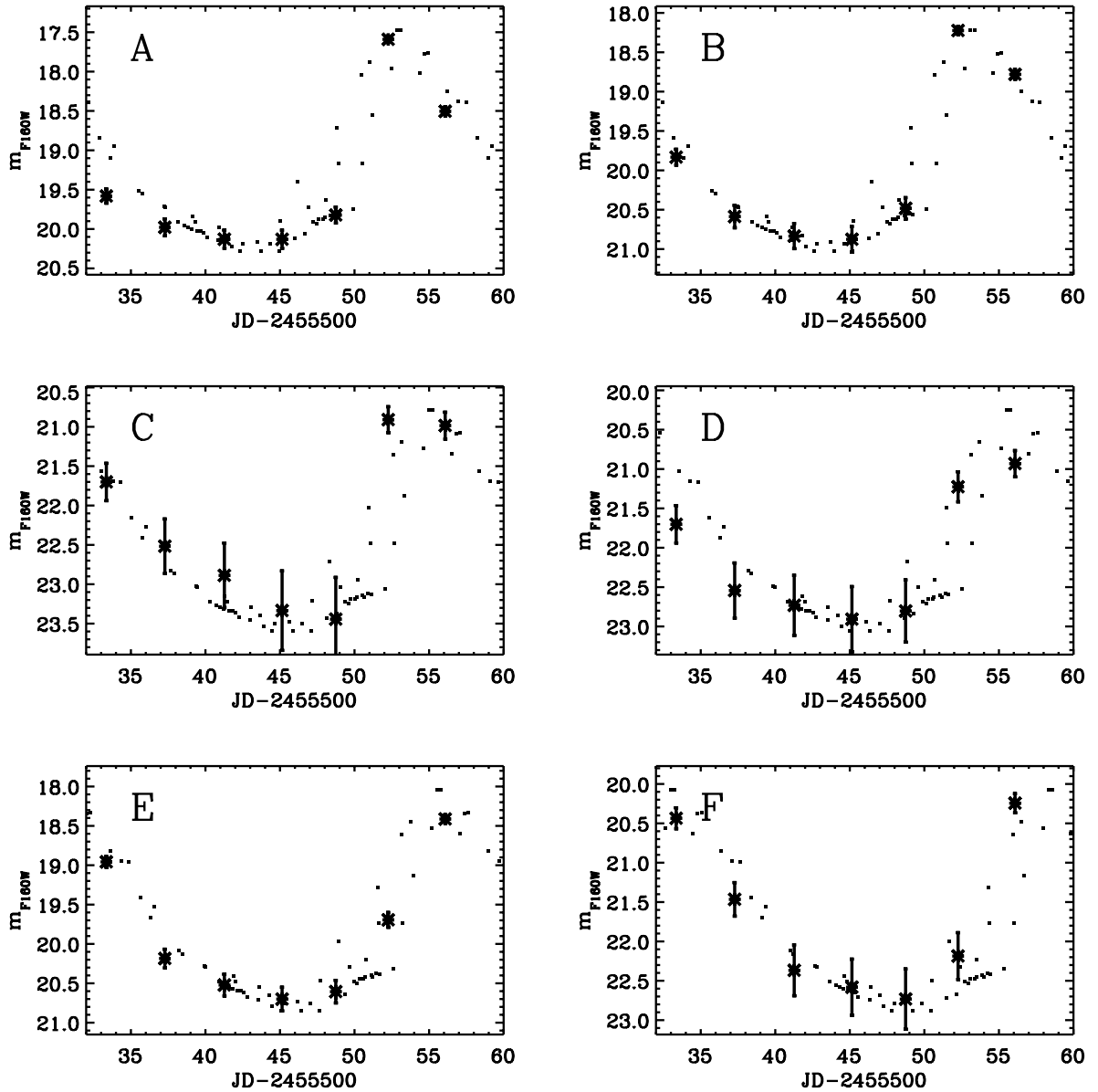


Figure S5. Aperture photometry of six regions from HST/WFC-IR F160W images of LRL 54361 (asterisks with error bars) as a function of observation time. Each panel shows the aperture magnitudes corresponding to the labeled region shown in Figure S4. The small squares show all warm Spitzer/IRAC 3.6 micron magnitudes, offset to match the F160W magnitude range. The Spitzer epochs were phased by the period of 25.34 days and then shifted with respect to the HST observing times by the following lags, calculated as described in the text: 0.51 days (A), 0.75 days (B), 2.65 days (C), 3.16 days (D), 3.22 days (E), 5.98 days (F).

28. Gutermuth, R. A., Megeath, S. T., Myers, P. C., Allen, L. E., Pipher, J. L., & Fazio, G. G. A Spitzer Survey of Young Stellar Clusters within one Kiloparsec of the Sun: Cluster Core Extraction and Basic Structural Analysis. *Astrophys. J. Suppl. Ser.* 184, 18-83 (2009)
29. Higdon et al. The SMART Data Analysis Package for the Infrared Spectrograph on the Spitzer Space Telescope. *PASP* 116, 975-984 (2004)
30. Lebouteiller, Bernard-Salas, Sloan & Barry. Advanced Optimal Extraction for the Spitzer/IRS. *PASP* 122, 888 (2010)
31. Reegen, P. SigSpec. I. Frequency- and phase-resolved significance in Fourier space. *Astron. Astrophys.* 467, 1353-1371 (2007)
32. Horne, J. H. & Baliunas, S. L. A prescription for period analysis of unevenly sampled time series. *Astrophys. J.* 302, 757-763 (1986)
33. Eisloffel, J., Froebrich, D., Stanke, T., & McCaughrean, M. J. Molecular Outflows in the Young Open Cluster IC 348. *Astrophys. J.* 595, 259-265 (2003)
34. Walawender, J., Bally, J., Kirk, H., Johnstone, D., Reipurth, B., & Aspin, C. Multiple Outflows and Protostars near IC 348 and the Flying Ghost Nebula. *Astron. J.* 132, 467-477 (2006)
35. Muench, A. A., Lada, C. J., Luhman, K. L., Muzerolle, J., & Young, E. A Spitzer Census of the IC 348 Nebula. *Astrophys. J.* 671, 1820-1831 (2007)
36. Dwek, E. The infrared echo of a type II supernova with a circumstellar dust shell - Applications to SN 1979c and SN 1980k. *Astrophys. J.* 274, 175-183 (1983)
37. Herbst, W. Star Formation in IC 348. *Handbook of Star Forming Regions, Volume 1: The Northern Sky.* 372-389 (2008)
38. Scholz, R.-D. et al. IC 348 proper motion study from digitised Schmidt plates. *Astron. Astrophys. Suppl. Ser.* 137, 305-321 (1999)
39. Herbig, G. H. The Young Cluster IC 348. *Astrophys. J.*, 497, 736-758 (1998)
40. Terebey, S., Shu, F. H., & Cassen, P. The collapse of the cores of slowly rotating isothermal clouds. *Astrophys. J.* 286, 529-551 (1984)
41. Draine, B. T. & Lee, H. M. Optical properties of interstellar graphite and silicate grains. *Astrophys. J.* 285, 89-108 (1984)
42. Pollack, J. B., Hollenbach, D., Beckwith, S., Simonelli, D. P., Roush, T., & Fong, W. Composition and radiative properties of grains in molecular clouds and accretion disks. *Astrophys. J.* 421, 615-639 (1994)

43. Ehrenfreund, P., Boogert, A. C. A., Gerakines, P. A., Jansen, D. J., Schutte, W. A., Tielens, A. G. G. M., & van Dishoeck, E. F. A laboratory database of solid CO and CO₂ for ISO. *Astron. Astrophys.* 315, 341-344 (1996)
44. Osorio, M., D'Alessio, P., Muzerolle, J., Calvet, N., & Hartmann, L. A Comprehensive Study of the L1551 IRS 5 Binary System. *Astrophys. J.* 586, 1148-1161 (2003)
45. Furlan, E., et al. Spitzer IRS Spectra and Envelope Models of Class I Protostars in Taurus. *Astrophys. J. Suppl. Ser.* 176, 184-215 (2008)
46. Lada, C. J. *et al.* Spitzer Observations of IC 348: The Disk Population at 2-3 Million Years. *Astron. J.* 131, 1574-1607 (2006)
47. Jorgensen, J. K. *et al.* The Spitzer c2d Survey of Large, Nearby, Interstellar Clouds. III. Perseus Observed with IRAC. *Astrophys. J.* 645, 1246-1263 (2006)
48. Rebull, L. M. *et al.* The Spitzer c2d Survey of Large, Nearby, Interstellar Clouds. VI. Perseus Observed with MIPS. *Astrophys. J. Suppl. Ser.* 171, 447-477 (2007)